Trishear in 3D. Algorithms, implementation, and limitations

Nestor Cardozo*

Center for Integrated Petroleum Research, Realfagbygget, Allegaten 41, N-5007 Bergen, Norway

Abstract

The algorithms and implementation of pseudo-3D and true-3D trishear models are explained, including a strategy to model lateral fault propagation. I show that the pseudo-3D algorithm is adequate and sufficient to model trishear in three-dimensions. Although ad-hoc, the pseudo-3D algorithm preserves volume in simulations without and with lateral fault propagation. A disadvantage of the pseudo-3D algorithm is that it produces very simple, and perhaps not realistic hanging wall geometries, specially in simulations in which the fault slip varies along strike. The true-3D algorithm has a more elaborate and richer kinematics that produces more realistic hanging wall geometries. However, the true-3D algorithm contains mathematical inconsistencies that result in considerable volume changes when the slip gradients along the tip line are high and the tip line is highly oblique to the slip vector and/or the fault strike. The volume changes occur to a large extent in the hanging wall, and to a minor extent in the forelimb and footwall areas.
© 2007 Elsevier Ltd. All rights reserved.

Keywords: Trishear; 3D; Fault propagation folding

1. Introduction

Trishear is a kinematic model of fault propagation folding in which the decrease in displacement along the fault is accommodated by heterogeneous shear in a triangular zone radiating from the tip line (Erslev, 1991; Allmendinger, 1998). The kinematics of the model in two-dimensions is well described by Zehnder and Allmendinger (2000). Thorough reviews of the model and its applications are given by Allmendinger et al. (2004) and Hardy and Allmendinger (submitted for publication).

Trishear has been extended to three-dimensions using two kind of formulations: a pseudo-3D formulation in which the model is solved in serial cross sections all parallel to the slip direction (Cristallini and Allmendinger, 2001), and a true-3D formulation in which the kinematics is solved in three-dimensions assuming volume conservation (Cristallini et al., 2004).

This note examines in detail the pseudo-3D and true-3D algorithms, their implementation, their limitations, and possible extensions such as lateral fault propagation. The pseudo-3D formulation is computationally less intensive than the true-3D formulation, and therefore this note also explores if the pseudo-3D formulation is sufficient to model trishear in three-dimensions.

I conclude that in most situations the pseudo-3D formulation is adequate to model trishear. Although the pseudo-3D algorithm is not a complete 3D implementation (but rather a two and a half implementation), the algorithm conserves volume within acceptable limits in all situations. The true-3D formulation is mathematically sounder and provides a richer kinematics in the hanging wall. However, volume changes in a true-3D model can be significant in models with high slip gradient along strike, such as lateral fault propagation.

The algorithms described in this note have been implemented in a computer program, Trishear3D. The program models the 3D geometry and finite strain of trishear fault related folds. Trishear3D is free for non-profit organizations, and can be downloaded at: http://homepage.mac.com/nfcd/work/programs.html. I encourage the reader to use the program to verify the ideas discussed here.

---

* Tel.: +47 5558 3693.
E-mail addresses: nestor.cardozo@cipr.uib.no, nfcd@mac.com

2. Algorithms

There are two main elements in a trishear formulation. The first is a description of the velocity field of the model (a snapshot of the deformation), and the second is a description of the evolution of the deformation (how the triangular zone of shear migrates through the rock material). In Section 2, I describe the velocity field of trishear according to the pseudo-3D and true-3D algorithms. In Section 3, I describe the evolution of the deformation.

2.1. Pseudo-3D

In the pseudo-3D algorithm (Cristallini and Allmendinger, 2001), trishear is solved in a series of cross sections, all parallel to the plane defined by the slip vector $\mathbf{v}(\mathbf{x})$ and the pole to the fault $\mathbf{y}$ (Fig. 1a, c). Within each $\mathbf{xy}$ cross section the model is solved using the simplest 2D kinematics, a symmetric trishear zone with v_x linear in $\mathbf{y}$ and concentration factor equal to one (Zehnder and Allmendinger, 2000, their Eqs. (2) and (6)).

The apical angle of the triangular zone of shear (trishear angle) and/or the slip are allowed to vary along the direction perpendicular to the slip vector ($\mathbf{z}$-axis, Fig. 1a). If the $\mathbf{x}$ (parallel to slip), $\mathbf{y}$ (parallel to the pole to the fault), and $\mathbf{z}$ (perpendicular to slip) coordinate system has origin at the tip T_s (Fig. 1a), the linear variation of trishear parameters along the $\mathbf{z}$-axis is expressed as:

$$A_t = \frac{(\varphi_n - \varphi_s)}{T_1'}, \quad \varphi = \varphi_s + A_t z \tag{1}$$

$$A_v = \frac{(v_n - v_s)}{T_1'}, \quad v = v_s + A_v z \tag{2}$$

where A_t and A_v are the coefficients of variation of trishear angle and slip, respectively, φ is half the trishear angle in radians (Fig. 1c), v is fault slip, T_1' is the distance between the fault tips along the $\mathbf{z}$-axis, and the s and n subscripts stand for the T_s and T_n tips (Fig. 1a).

Along an $\mathbf{xy}$ cross section (Fig. 1c) the velocity field is defined as:

$$v_x = v, \; v_y = 0, \quad \text{for } y \geq x_c m \tag{3}$$

$$v_x = 0, \; v_y = 0, \quad \text{for } y \leq -x_c m \tag{4}$$

$$v_x = \frac{v}{2}\left[\frac{y}{x_c m} + 1\right], \quad \text{for } x_c m \geq y \geq -x_c m \tag{5a}$$

$$v_y = \frac{mv}{4}\left[\left(\frac{y}{x_c m}\right)^2 - 1\right], \quad \text{for } x_c m \geq y \geq -x_c m \tag{5b}$$

where m is the tangent of φ, and x_c is the coordinate in x corrected by the difference between the $\mathbf{z}$-axis and the tip line:

$$x_c = x - \left(\frac{z}{T_{n,z}}\right)T_{n,x} \tag{6}$$
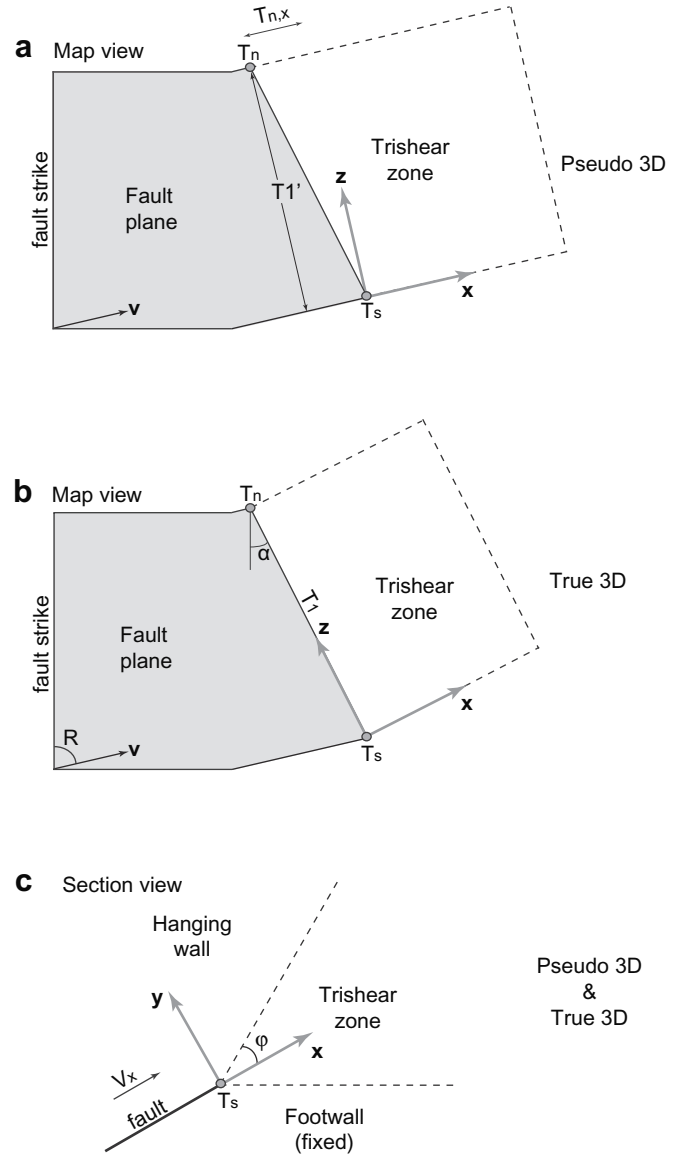
Fig. 1. Geometry of the pseudo-3D and true-3D trishear algorithms. T_s and T_n are the fault tips. (a) Map view of the pseudo-3D algorithm. $\mathbf{x}$ and $\mathbf{z}$ are parallel and perpendicular to the slip vector $\mathbf{v}$, respectively. (b) Map view of the true-3D algorithm. $\mathbf{x}$ and $\mathbf{z}$ are perpendicular and parallel to the tip line, respectively. (c) Cross section of the pseudo-3D and true-3D algorithms. $\mathbf{y}$ is the pole of the fault. The line of section passes along the tip T_s but its orientation ($\mathbf{x}$-axis) in the pseudo-3D and true-3D algorithms is different. Other symbols are explained in the text.

$T_{n,x}$ and $T_{n,z}$ are the x and z coordinates of the tip T_n (Fig. 1a). The hanging wall area above the triangular zone of shear translates with a velocity v (Eq. (3)), the footwall area below the triangular zone is fixed (Eq. (4)), and particles inside the triangular zone move according to Eq. (5). Notice that Eqs. (3)–(5) are compatible at the boundaries of the triangular zone ($y = x_c m$ and $y = -x_c m$). Along an $\mathbf{xy}$ cross section the velocity vectors look like Fig. 2a (left and middle).

The pseudo-3D formulation is an ad-hoc extension of the 2D formulation. There is no mathematical proof of volume conservation. The fundamental assumption of the algorithm is that there is no movement along the $\mathbf{z}$-axis (perpendicular
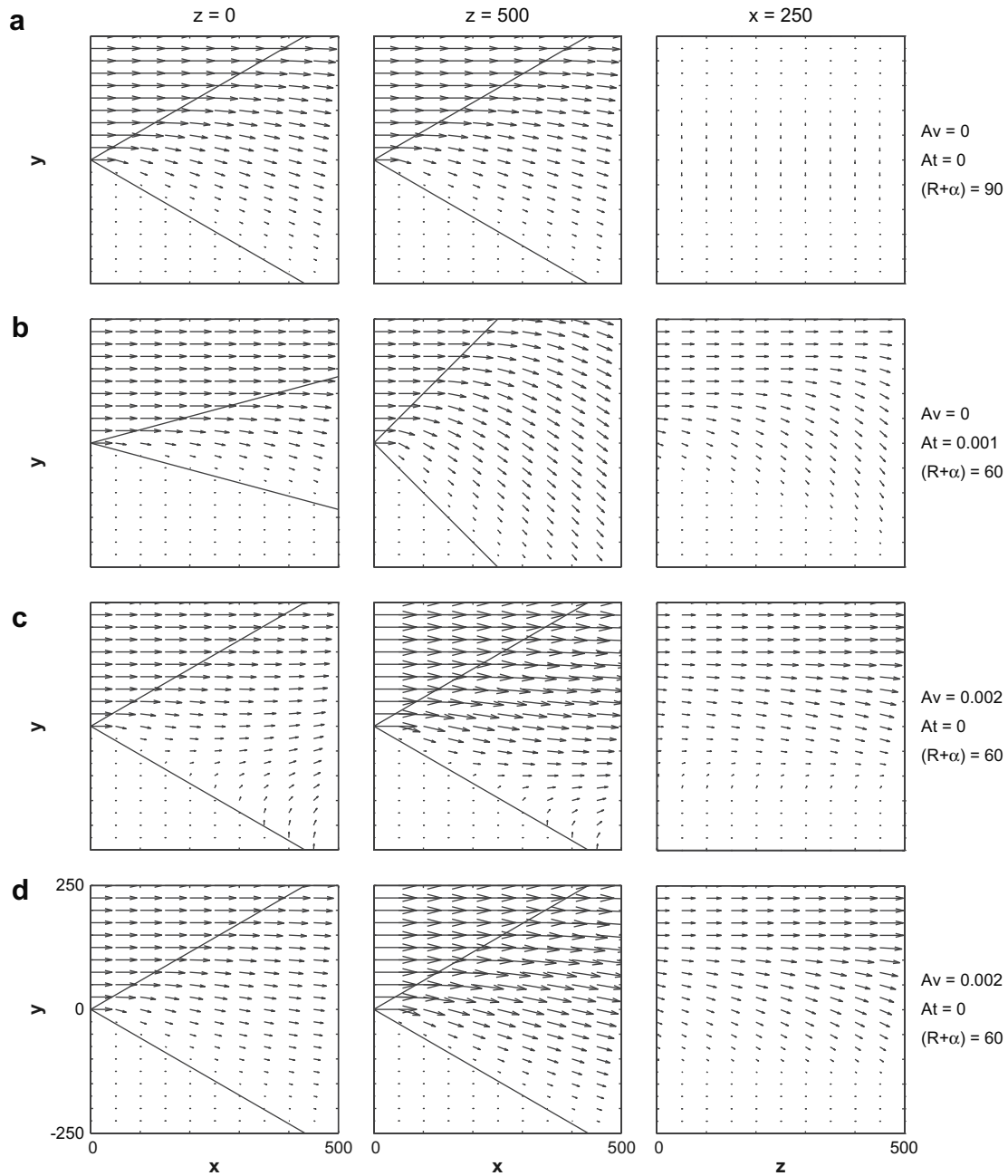
Fig. 2. Velocity fields of the true-3D algorithm. (a) Simplest velocity field with no variation of slip or trishear angle, and $(R + \alpha)$ equal to 90°. This velocity field is similar to the velocity field of the pseudo-3D algorithm. (b) Velocity field with variation of trishear angle along the tip line and $(R + \alpha)$ equal to 60°. (c) Velocity field with variation of slip along the tip line and $(R + \alpha)$ equal to 60°. Velocity field was computed using Eqs. (22) and (23). (d) Similar to (c) but velocity field computed using Eqs. (24) and (25). In all cases the velocity vectors are exaggerated 50 times.

to the slip vector, Fig. 2a, right). This might not ensure volume conservation. However, Cristallini and Allmendinger (2001) show that pseudo-3D models with variable trishear parameters conserve volume within reasonable limits. I reach similar conclusions in Section 4.3.

2.2. True-3D

In the true-3D algorithm (Cristallini et al., 2004), the kinematics of trishear is solved in three-dimensions using the

principle of volume conservation. Cristallini et al. (2004) describes in detail the equations of the true-3D algorithm. In this section, I will go over Cristallini et al. (2004) derivation in order to understand the true-3D algorithm but also to point out some problems with the formulation.

The true-3D algorithm is based on an **xyz** coordinate system with **x** perpendicular to the tip line, **y** perpendicular to the fault plane (i.e. pole to the fault), and **z** parallel to the tip line. The origin of this coordinate system is at the tip T_s (Fig. 1b, c). As well as in the pseudo-3D algorithm, a symmetric trishear zone

is assumed (Fig. 1c). Along the tip line (**z**-axis), linear changes in trishear angle, and/or slip are allowed:

$$A_t = \frac{(\varphi_n - \varphi_s)}{T_1}, \quad \varphi = \varphi_s + A_t z \tag{7}$$

$$A_v = \frac{(v_n - v_s)}{T_1}, \quad v = v_s + A_v z \tag{8}$$

where T_1 is the length of the tip line (Fig. 1b), and the other symbols are as above. Notice that in the pseudo-3D algorithm, the variation of the trishear parameters is defined along the direction perpendicular to the slip vector (Eqs. (1) and (2)), while in the true-3D algorithm, the variation of the parameters is defined along the tip line (Eqs. (7) and (8)).

In the hanging wall and footwall regions outside the triangular zone of shear (Fig. 1c), the velocity field is defined by the following equations:

$$v_x = v\sin(R + \alpha), \quad v_y = 0, \quad v_z = v\cos(R + \alpha), \quad \text{for } y \geq xm \tag{9}$$

$$v_x = 0, \quad v_y = 0, \quad v_z = 0, \quad \text{for } y \leq -xm \tag{10}$$

where R is the angle between the slip vector and the fault strike, and α is the angle between the tip line and the fault strike (Fig. 1b). Both angles, R and α, are measured on the fault plane and are expressed in radians. The hanging wall area above the triangular zone translates with a velocity v (Eq. (9)), and the footwall area below the triangular zone is fixed (Eq. (10), Fig. 1c).

Inside the triangular zone of deformation ($xm \geq y \geq -xm$), the simplest linear in **y** velocity field is assumed for the v_x and v_z velocities:

$$v_x = \frac{v_{a,x}}{2}\left[\frac{y}{xm} + 1\right] \tag{11}$$

$$v_z = \frac{v_{a,z}}{2}\left[\frac{y}{xm} + 1\right] \tag{12}$$

where $v_{a,x}$ and $v_{a,z}$ are the v_x and v_z velocities in the hanging wall area above the triangular zone (Eq. (9), Fig. 1c). Notice that Eqs. (9)–(12) are compatible at the boundaries of the triangular zone ($y = xm$ and $y = -xm$).

To find v_y inside the triangular zone, volume conservation (i.e. flow incompressibility) is applied:

$$\text{div } \mathbf{v} = \frac{\partial v_x}{\partial x} + \frac{\partial v_y}{\partial y} + \frac{\partial v_z}{\partial z} = 0 \tag{13}$$

The x term of Eq. (13) is easy to derive:

$$\frac{\partial v_x}{\partial x} = -\frac{v_{a,x}}{2}\frac{y}{x^2 m} = -\frac{v_{a,x}}{2}\frac{y}{x^2 \tan\varphi} \tag{14}$$

The z term of Eq. (13) is more difficult to derive, since both $v_{a,z}$ and m vary along the **z**-axis. Using Eqs. (7)–(9); Eq. (12) can be rewritten as:

$$v_z = \frac{[v_s + (A_v z)]\cos(R + \alpha)}{2}\left[\frac{y}{x\tan[\varphi_s + (A_t z)]} + 1\right] \tag{15}$$

For convenience let's call the first factor of Eq. (15) A_z, and the second factor B_z. The partial derivative of v_z with respect to z is then:

$$\frac{\partial v_z}{\partial z} = A_z' B_z + A_z B_z' \tag{16}$$

$$A_z' = \frac{A_v \cos(R + \alpha)}{2} \tag{17}$$

$$B_z' = -\frac{y}{x} J_z \tag{18}$$

$$J_z = \frac{A_t}{\tan^2\varphi \cos^2\varphi} \tag{19}$$

Eqs. (16)–(19) correspond to Eqs. (13)–(16) of Cristallini et al. (2004). The reader should be aware that there are typographical errors in Eqs. (15) and (16) of Cristallini et al. (2004). We now have all terms to compute the partial derivative of v_y with respect to y. Using Eqs. (13)–(19):

$$\frac{\partial v_y}{\partial y} = -\frac{\partial v_x}{\partial x} - \frac{\partial v_z}{\partial z} \tag{20}$$

$$\frac{\partial v_y}{\partial y} = \frac{v_{a,x}y}{2x^2 \tan\varphi} - A_z'\left[\frac{y}{x\tan\varphi} + 1\right] + A_z J_z\frac{y}{x} \tag{21}$$

v_y can be computed by integrating Eq. (21) in y:

$$v_y = \frac{v_{a,x}y^2}{4x^2\tan\varphi} - \frac{A_z'y^2}{2x\tan\varphi} - A_z'y + \frac{A_z J_z y^2}{2x} + C \tag{22}$$

Eqs. (21) and (22) correspond to Eqs. (18) and (19) of Cristallini et al. (2004). Again, there are typographical errors in Eqs. (18) and (19) of Cristallini et al. (2004) publication.

The constant of integration C can be found by applying the condition that v_y is zero at the upper ($y = xm$) and lower ($y = -xm$) boundaries of the triangular zone (Eqs. (9) and (10), Fig. 1c). However, an examination of Eq. (22) reveals a fundamental problem. Eq. (22) is not symmetric in y. The third term of this equation is a function of y rather than y^2. This means that there is not a unique value of C that satisfies the velocity in y condition at both, the upper and the lower boundaries of the triangular zone.

Cristallini et al. (2004) use a value of C that honors the velocity conditions at the upper boundary of the triangular zone (Cristallini, personal communication):

$$C = -\frac{v_{a,x}\tan\varphi}{4} + \frac{A_z'x\tan\varphi}{2} + A_z'x\tan\varphi - \frac{A_z J_z x\tan^2\varphi}{2} \tag{23}$$

Another alternative is to disregard the third term of Eq. (22):

$$v_y = \frac{v_{a,x}y^2}{4x^2\tan\varphi} - \frac{A_z'y^2}{2x\tan\varphi} + \frac{A_z J_z y^2}{2x} + C \tag{24}$$

$$C = -\frac{v_{a,x}\tan\varphi}{4} + \frac{A_z'x\tan\varphi}{2} - \frac{A_zJ_zx\tan^2\varphi}{2} \qquad (25)$$

Both approaches are mathematically incorrect when A_z' is not zero. Another problem of the true-3D algorithm is that the volume is not always preserved in the hanging wall region outside the triangular zone. The divergent (Eq. (13)) of the velocity field in the hanging wall region above the triangular zone (Eq. (9)) is not zero, but rather $A_v\cos(R + \alpha)$. In the true-3D algorithm, volume is not preserved neither in the triangular zone nor in the hanging wall region above it, when the slip varies along the fault ($A_v \neq 0$), and the tip line is oblique to the slip vector and/or the fault strike ($R + \alpha$ is not 90 or 270°). In this situation A_z' (Eq. (17)) is not zero.

Fig. 2a shows the velocity field of a true-3D model with no variation of slip or trishear angle along the tip line ($A_v = 0$, $A_t = 0$), and ($R + \alpha$) equal to 90°. In this case, v_z, A_z, A_z', and J_z are all zero and Eqs. (11), (12) and (22) reduce to Eq. (5), which is the velocity field of the pseudo-3D model. In fact, as long as ($R + \alpha$) is 90°, the pseudo-3D and true-3D formulations are the same, even in cases in which the trishear angle and/or the slip varies along the tip line ($A_t \neq 0$, $A_v \neq 0$). The model of Fig. 2a is mathematically correct and preserves volume.

Fig. 2b shows a more interesting true-3D model. The trishear angle varies from 30 to 90° along a 500 units long tip line ($A_t = 0.001$), ($R + \alpha$) is 60°, and slip is constant ($A_v = 0$). In this model there is movement along the **z** direction (Fig. 2b right) and A_z and J_z are not zero. Compared to true-3D models with ($R + \alpha$) equal to 60° and no trishear angle variation, the component of the velocity in the $-y$ direction is enhanced in the triangular zone in the variable trishear angle model (Fig. 2b). This case is mathematically correct and preserves volume. There are contributions from the A_z and J_z terms, but no contribution from the A_v and A_z' terms.

Fig. 2c, d show the velocity field of a true-3D model in which the slip varies from 1.0 to 2.0 along a 500 units long tip line ($A_v = 0.002$), ($R + \alpha$) is 60°, and trishear angle is 60° and is constant ($A_t = 0$). Fig. 2c was computed using Eqs. (22) and (23) and Fig. 2d using Eqs. (24) and (25). A_z' in this model is non-zero and there is movement along the **z** direction (Fig. 2c, d right). If the A_z' term in y of Eq. (22) is considered (Fig. 2c), the component of the velocity in the **y** direction is enhanced in the triangular zone (compare Fig. 2a, c). The velocity field is correct for $y \geq 0$, but incorrect for $y < 0$. At the lower boundary of the triangular zone, the velocity vectors are incompatible with the fixed condition of the footwall (Fig. 2c). If the A_z' term in y of Eq. (22) is disregarded (Fig. 2d), the increase of the velocity in the **y** direction is not as significant as in the model of Fig. 2c, particularly in the lower half of the triangular zone, and there are no velocity incompatibilities at the boundaries of the triangular zone. The differences between the models of Fig. 2c, d are more significant in the lower half of the triangular zone, and in regions of the upper half of the triangular zone with high x values.

As discussed before, models such as those of Fig. 2c, d are not mathematically correct and do not preserve volume. In Section 4.3, I discuss the volume changes involved in such models. In some cases, the volume changes are small and to an extent acceptable. In other cases, the volume changes are significant, particularly when the gradient of slip A_v is high, and the tip line is highly oblique to the slip vector and/or to the fault strike.

3. Implementation

Given the velocity field, the resultant deformation can be computed by incrementally moving the triangular zone of shear through the rock material. The movement of the triangular zone is defined by the rate of fault propagation to fault slip (*P/S*). As well as the other trishear parameters, the *P/S* can vary along the **z**-axis.

For both the pseudo-3D and true-3D formulations, the simulation of the deformation involves transforming the coordinates of each particle from a reference east-north-up (**enu**) coordinate system, to an **x′y′z′** stationary coordinate system with origin at the initial location of the tip T_s (T_{so}), and finally to an **xyz** mobile coordinate system with origin at the current location of the tip T_s (Fig. 3a, b).

Once the particles are in the **xyz** coordinate system, their velocities are computed using the equations of Section 2, and their positions are updated. This is done every increment of slip. At the end of the deformation, the particles are transformed back to the **enu** coordinate system and plotted for visualization.

3.1. Pseudo-3D

In the pseudo-3D implementation, the stationary **x′y′z′** and mobile **xyz** coordinate systems have similar orientation, with **x** parallel to the slip vector, **y** perpendicular to the fault, and **z** perpendicular to the slip vector (Fig. 3a). The variation of *P/S* along the **z**-axis (perpendicular to the slip vector), is defined by:

$$A_p = \frac{((P/S)_n - (P/S)_s)}{T_1'}, \quad (P/S) = (P/S)_s + A_p z \qquad (26)$$

The transformation between the stationary **x′y′z′** and mobile **xyz** coordinate systems is:

$$x = x' - (P/S)_s|v_s|i, \quad y = y', \quad z = z' \qquad (27)$$

where i is the number of slip increments. To compute the velocity field using Eqs. (3)–(5), x should be corrected for the variation of *P/S* along the **z**-axis, and the difference between the **z**-axis and the initial orientation of the tip line:

$$x_c = x + [(P/S)_s|v_s|i - (P/S)|v|i] - \left(\frac{z}{T_{no,z}}\right)T_{no,x'} \qquad (28)$$

which reduces to:

$$x_c = x' - (P/S)|v|i - \left(\frac{z}{T_{no,z}}\right)T_{no,x'} \qquad (29)$$
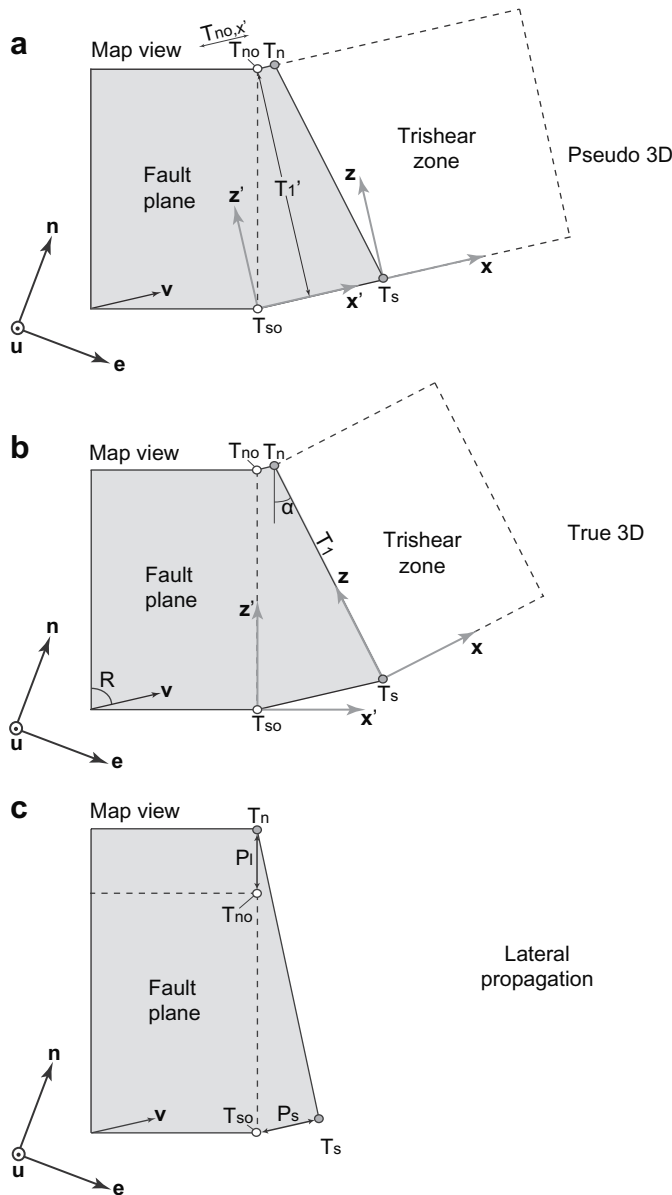
Fig. 3. Implementation of the (a) Pseudo-3D algorithm, (b) true-3D algorithm, and (c) lateral fault propagation. In all cases the **enu** is a reference coordinate system used for plotting. In a and b the **x′y′z′** is a stationary coordinate system with origin at the initial location of the tip T_s (T_{so}), and the **xyz** is a mobile coordinate system with origin at the tip T_s. The solution involves transforming particles from the **enu** to the **x′y′z′** and to the **xyz** coordinate system, computing the velocity and updating the position of the particles in the **xyz** coordinate system, and transforming back the particles to the **enu** coordinate system for plotting. Other symbols are explained in the text.

where $T_{no,x'}$ and $T_{no,z}$ are the x' and z coordinates of the initial location of the tip T_n (T_{no} in Fig. 3a).

There are three things to keep in mind with regard to the pseudo-3D implementation: (i) The stationary **x′y′z′** and mobile **xyz** coordinate systems are coaxial, (ii) The orientation of the mobile **xyz** coordinate system does not change throughout the deformation, and (iii) T'_1 and the variation of trishear parameters A_t, A_v, A_p, remain constant throughout the deformation. These characteristics save considerable computation time: (i) T'_1, A_t,

A_v, and A_p can be computed before the deformation, (ii) The only parameter that needs to be updated every increment of slip is x_c (Eq. (29)), and (iii) The velocity field can be directly used to update the position of particles in the stationary **x′y′z′** coordinate system.

Another feature that is convenient about the pseudo-3D model, is that neither the stationary **x′y′z′** nor the mobile **xyz** coordinate systems are related to the tip line. This makes easy to introduce more elaborate variations of trishear parameters than those of Eqs. (1), (2) and (26). For example, in my Trishear3D program in addition to the standard variation of trishear parameters (Eqs. (1), (2) and (26)), I implemented a bi-linear variation of trishear parameters, from the tips to the mid-point of the tip line. Other programs (i.e. Cristallini's Trishear in 3D program) allow the user to digitize the variation of trishear parameters along fault strike.

3.2. True-3D

In the true-3D implementation, the stationary **x′y′z′** and mobile **xyz** coordinate systems have different orientations. The stationary **x′y′z′** coordinate system has axes parallel to the fault up-dip direction (**x′**), perpendicular to the fault (**y′**), and parallel to the fault strike (**z′**, Fig. 3b). The mobile **xyz** coordinate system has axes perpendicular to the tip line (**x**), perpendicular to the fault (**y**), and parallel to the tip line (**z**, Fig. 3b). The mobile **xyz** coordinate system is attached to the tip line, and therefore its orientation can vary throughout the deformation.

The first part of the implementation consists of finding in the stationary **x′y′z′** coordinate system, the current length (T_1) and orientation with respect to the fault strike of the tip line (α, Fig. 3b). For convenience, let's call the propagation of the T_s and T_n tips P_s and P_n, respectively:

$$P_s = (P/S)_s |v_s| i \tag{30a}$$

$$P_n = (P/S)_n |v_n| i \tag{30b}$$

The x', z' coordinates of the T_s and T_n tips (Fig. 3b) are:

$$T_{s,x'} = P_s \cos\left(\frac{\pi}{2} - R\right) \tag{31a}$$

$$T_{s,z'} = P_s \cos(R) \tag{31b}$$

$$T_{n,x'} = T_{no,x'} + P_n \cos\left(\frac{\pi}{2} - R\right) \tag{31c}$$

$$T_{n,z'} = T_{no,z'} + P_n \cos(R) \tag{31d}$$

where $T_{no,x'}$ and $T_{no,z'}$ are the x' and z' coordinates of the initial location of the tip T_n (T_{no} in Fig. 3b). The length T_1 of the tip line (Fig. 3b) is:

$$T_1 = \sqrt{(T_{n,x'} - T_{s,x'})^2 + (T_{n,z'} - T_{s,z'})^2} \tag{32}$$

The angle α that the tip line makes with the fault strike (Fig. 3b) is:

$$\alpha = \arctan\left(\frac{T_{s,x'} - T_{n,x'}}{T_{n,z'} - T_{s,z'}}\right) \tag{33}$$

The transformation between the stationary $\mathbf{x'y'z'}$ coordinate system and the mobile $\mathbf{xyz}$ coordinate system (Fig. 3b) is:

$$x = (x' - T_{s,x'})\cos(\alpha) + (z' - T_{s,z'})\cos\left(\frac{\pi}{2} - \alpha\right) \tag{34a}$$

$$y = y' \tag{34b}$$

$$z = (x' - T_{s,x'})\cos\left(\frac{\pi}{2} + \alpha\right) + (z' - T_{s,z'})\cos(\alpha) \tag{34c}$$

Once the particles are in the mobile $\mathbf{xyz}$ coordinate system, their velocities are computed using Eqs. (9)–(12) and Eqs. (22) or (24), and their positions are updated.

By comparison to the pseudo-3D implementation, the true-3D implementation is more elaborate: (i) The mobile $\mathbf{xyz}$ coordinate system can change progressively in orientation with deformation, (ii) The orientation and length of the tip line can change progressively in orientation with deformation and therefore T_1, α, A_t, and A_v should be computed every increment of slip, and (iii) Contrary to the pseudo-3D implementation, the transformation between the stationary $\mathbf{x'y'z'}$ and mobile $\mathbf{xyz}$ coordinate system involves more than just a simple translation. Updated particle positions in the mobile $\mathbf{xyz}$ coordinate system should be transformed back to the stationary $\mathbf{x'y'z'}$ coordinate system.

The true-3D implementation is therefore more computationally intensive than the pseudo-3D implementation. In Trishear3D, true-3D models take twice as long as pseudo-3D models. Also the fact that the $\mathbf{xyz}$ coordinate system of the true-3D algorithm is attached to the tip line makes it impossible to implement more complex variations of trishear parameters along the tip line than the linear variation between the tips of Eqs. (7) and (8).

3.3. Lateral fault propagation

An interesting extension of the pseudo-3D and true-3D implementations is lateral fault propagation. In this case, the fault propagates and grows in length across and along strike (Fig. 3c). The slip on one of the fault tips is non-zero (T_s in Fig. 3c) and the slip on the tip that propagates along strike (but not across strike) is set to zero (T_n in Fig. 3c). During deformation, the propagation along strike P_l (Fig. 3c) is:

$$P_l = (P/S)_l |v_t| i \tag{35}$$

where $(P/S)_l$ is the lateral propagation to slip ratio, and v_t is the slip at the tip that propagates across strike (T_s in Fig. 3c). The tip line grows in length with deformation, and therefore in the pseudo-3D implementation, T_1' and the variation of the trishear parameters along the $\mathbf{z}$-axis, A_t, A_v, and A_p, need to be updated every increment of slip:

$$T_1' = T_{\text{no},z} + P_l \sin(R) \tag{36}$$

where $T_{\text{no},z}$ is the z coordinate of the initial location of the tip T_n (T_{no} in Fig. 3c). Once T_1' is known, A_t, A_v, and A_p are updated using Eqs. (1), (2) and (26). If the tip T_n moves along strike (like in Fig. 3c), the trishear parameters for a given particle are computed using the right side of Eqs. (1), (2) and (26). If on the other hand the tip T_s (which is the origin of the $\mathbf{xyz}$ coordinate system) moves along strike, the trishear parameters should be computed using as reference the tip T_n:

$$\varphi = \varphi_n - A_t(T_{n,z} - z) \tag{37}$$

$$v = v_n - A_v(T_{n,z} - z) \tag{38}$$

$$(P/S) = (P/S)_n - A_p(T_{n,z} - z) \tag{39}$$

where $T_{n,z}$ is the coordinate in z of the tip T_n. This strategy avoids performing additional transformations of the $\mathbf{xyz}$ coordinate system. Compared to the standard pseudo-3D formulation (Section 3.1), the extra burden of lateral fault propagation is computing the distance between the fault tips and the variation of trishear parameters along the $\mathbf{z}$-axis every increment of slip.

In the true-3D formulation, lateral fault propagation is introduced when computing the positions of the fault tips in the stationary $\mathbf{x'y'z'}$ coordinate system. For example if, as in Fig. 3c, the tip T_n propagates along strike, Eq. (31) becomes:

$$T_{s,x'} = P_s \cos\left(\frac{\pi}{2} - R\right) \tag{40a}$$

$$T_{s,z'} = P_s \cos(R) \tag{40b}$$

$$T_{n,x'} = T_{\text{no},x'} \tag{40c}$$

$$T_{n,z'} = T_{\text{no},z'} + P_l \tag{40d}$$

where $T_{\text{no},x'}$ and $T_{\text{no},z'}$ are the x' and z' coordinates of the initial location of the tip T_n (T_{no} in Fig. 3c). After this, the solution is similar to the standard true-3D implementation (Eqs. (32)–(34)).

4. Modeling

In Section 4, I compare pseudo-3D and true-3D trishear models. I also check the validity of the models in terms of volume conservation. All models have initially horizontal beds and horizontal fault tip line (α is 0). Additionally the slip is perpendicular to the fault strike (R is 90°). Under these conditions the $\mathbf{xyz}$ coordinate systems of the pseudo-3D and true-3D models (Fig. 3a, b) are the same at the beginning of the deformation.

4.1. No lateral fault propagation

Figs. 4 and 5 show vertical cross sections across pseudo-3D (black lines) and true-3D (gray lines) trishear models of reverse (Fig. 4) and normal (Fig. 5) faults propagating in the up-dip direction. The length of the fault along strike is 500 units and the cross sections are perpendicular to strike and are drawn at the T_s ($n = 0$) and T_n ($n = 500$ units) fault tips. The reverse fault dips 30° (Fig. 4), and the normal fault 60° (Fig. 5). The
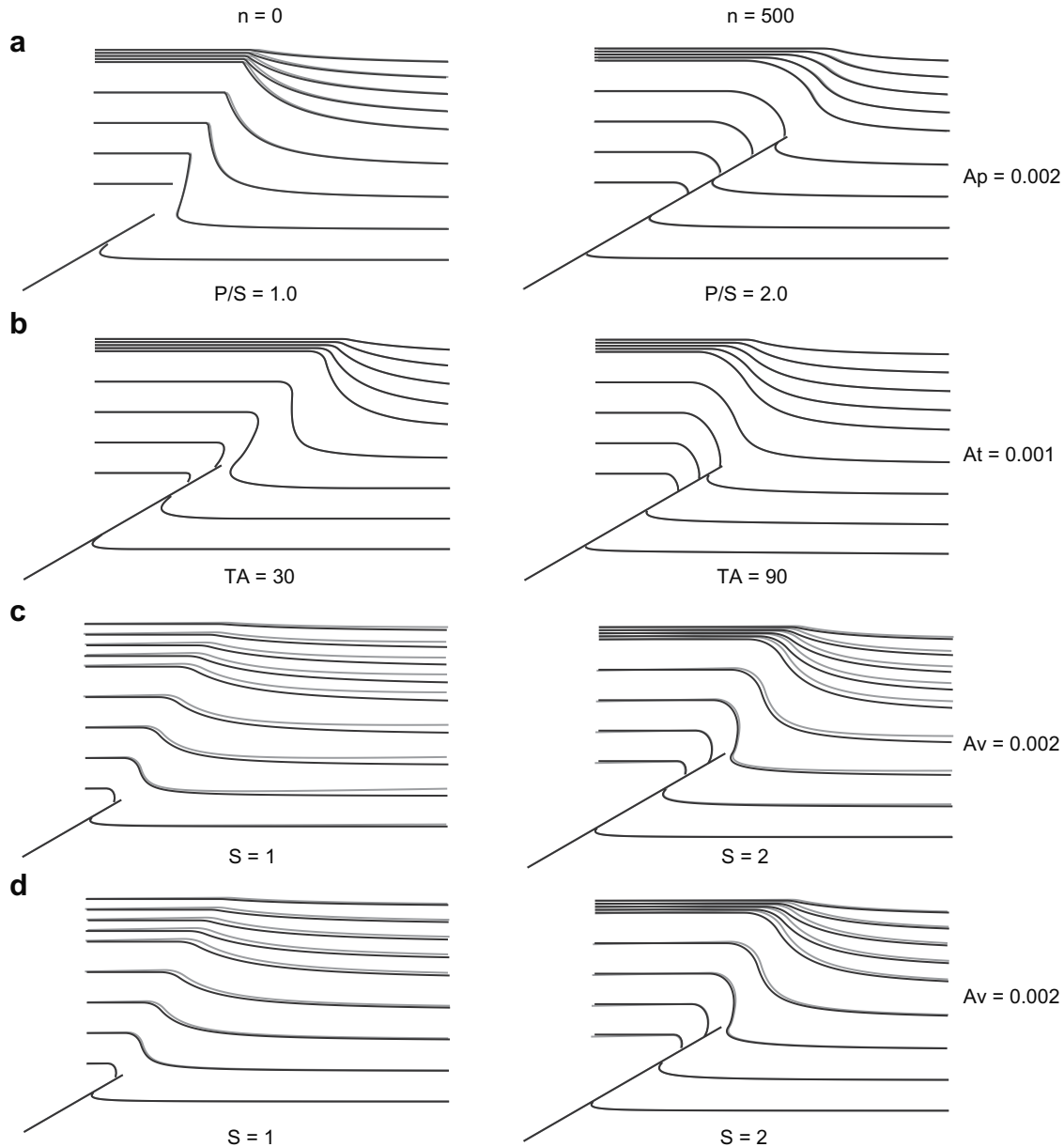
Fig. 4. Vertical cross sections across pseudo-3D (black lines) and true-3D (gray lines) trishear models of a 30° dipping, reverse fault with (a) variable *P/S*, (b) variable trishear angle, and (c, d) variable slip. In (c) the true-3D model was computed using Eqs. (22) and (23), and in (d) using Eqs. (24) and (25). All models are 500 units along the fault strike. Cross sections are perpendicular to the fault strike and are located at the frontal ($n = 0$) and rear ($n = 500$ units) face of the models. Lower five beds are pre-growth, and upper four beds are growth strata.

lower five beds are pre-growth, and the upper four beds are growth strata.

Fig. 4a illustrates a reverse fault model with variable *P/S*. The trishear angle is 60°, the total, cumulative slip is 250 units accumulated over 125 increments (slip = 2 units), and the *P/S* varies from 1.0 at T_s to 2.0 at T_n ($A_p = 0.002$). In the cross section at $n = 0$ (Fig. 4a left side), the pseudo-3D model (black lines) shows a distinct kink in the pre-growth and growth strata, typical of trishear models with *P/S* = 1 (Allmendinger, 1998). This geometry is also exhibited by the true-3D model (gray lines), but the angularity and tightness of the anticlinal hinge slightly decrease up-section from the pre-growth to the growth strata. In the cross section at $n = 500$ units (Fig. 4a

right side), the pseudo-3D geometry (black lines) consists of a broad anticline and syncline cut by the fault. The true-3D geometry (gray lines) is very similar, with the exception of minor differences in the growth strata. The slight differences between the pseudo-3D and true-3D models are due to the different orientation of the **xyz** coordinate system of these models. Contrary to the pseudo-3D model, the orientation of **xyz** changes progressively with deformation in the true-3D model, because T_n propagates faster than T_s. In the pseudo-3D model, the $n = 0$ and $n = 500$ units cross sections are aligned with the **x**-axis, and *P/S* is constant in the sections. In the true-3D model, the $n = 0$ and $n = 500$ units cross sections are not aligned with the **x**-axis, and *P/S* is not constant in the sections
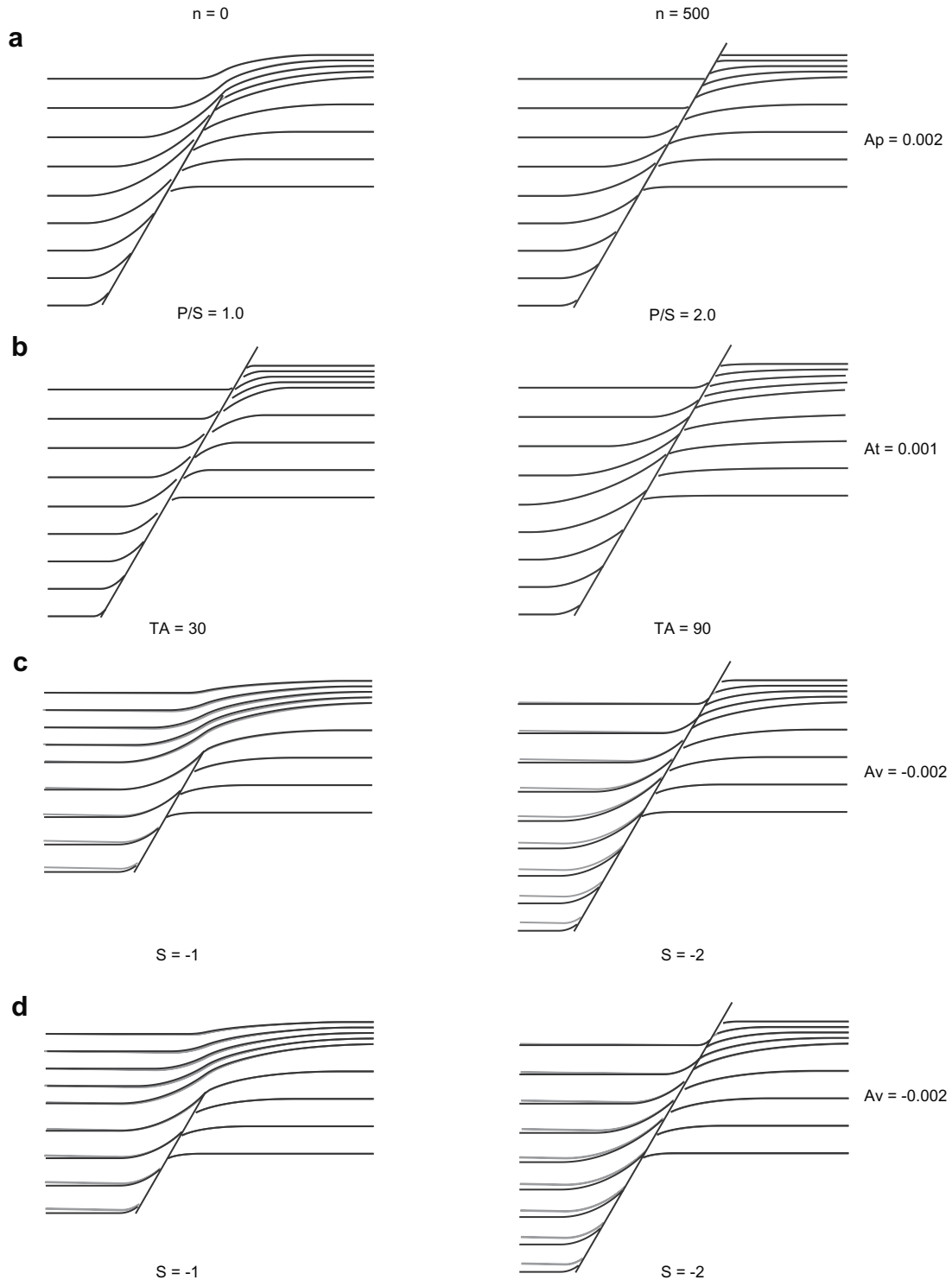
Fig. 5. Vertical cross sections across pseudo-3D (black lines) and true-3D (gray lines) trishear models of a 60° dipping, normal fault with (a) variable *P/S*, (b) variable trishear angle, and (c, d) variable slip. In (c) the true-3D model was computed using Eqs. (22) and (23), and in (d) using Eqs. (24) and (25). All models are 500 units along the fault strike. Cross sections are perpendicular to the fault strike and are located at the frontal (*n* = 0) and rear (*n* = 500 units) face of the models. Lower five beds are pre-growth, and upper four beds are growth strata.

but rather increases up-section. Also the length of the tip line T_1 increases with deformation, such that A_p is not constant but rather decreases with deformation. *P/S* variations in a cross section have more influence in the resultant fold geometry at

low *P/S* (around 1.0, Fig. 4a left side) than at high *P/S* (around 2.0, Fig. 4a right side) values.

Fig. 4b illustrates a reverse fault model with variable trishear angle. The *P/S* is 1.5, the total slip is 250 units

accumulated over 125 increments (slip = 2 units), and the trishear angle varies from 30° at T_s to 90° at T_n ($A_t = 0.001$). The resultant folds become wider and the fold hinges more rounded as the trishear angle increases along the fault from T_s (Fig. 4b left side) to T_n (Fig. 4b right side). In this case the pseudo-3D (black lines) and true-3D (gray lines) geometries are the same. A_t is not zero, but throughout the deformation $(R + \alpha)$ is 90°, and the velocity equations of the true-3D model reduce to those of the pseudo-3D model (Section 2). Another scenario in which this can happen is when the slip vector is perpendicular to the fault, the tip line before the deformation is horizontal, and the P/S is zero (no fault propagation). In this case, $(R + \alpha)$ remains 90 or 270° throughout the deformation, even if the slip along strike varies ($A_v \neq 0$).

Fig. 4c, d show a reverse fault model with variable slip. The P/S is 1.5, the trishear angle is 60°, and the total slip varies from 125 units at T_s to 250 units at T_n. The total slip is reached over 125 increments. The slip varies therefore from 1 unit at T_s to 2 units at T_n ($A_v = 0.002$). In Fig. 4c the true-3D model was computed using Eqs. (22) and (23), and in Fig. 4d using Eqs. (24) and (25). Similar to the variable P/S simulation (Fig. 4a), differences in the geometry between the pseudo-3D (black lines) and true-3D (gray lines) models in the variable slip simulation (Fig. 4c, d) are partially due to the different orientation of the **xyz** coordinate systems of these models. In the pseudo-3D model the orientation of the **xyz** coordinate system does not change with deformation, but in the true-3D model the **xyz** coordinate system rotates progressively with deformation because T_n propagates more than T_s. Slip is not constant in the $n = 0$ and $n = 500$ cross sections but rather increases up-section. Also the length of the tip line T_1 increases with deformation, such that A_v is not constant but rather decreases with deformation. But additionally to this, since A_v is not zero and $(R + \alpha)$ is not 90°, the differences between the pseudo-3D and true-3D models are also due to the contribution of the A_z' term in Eqs. (22) and (23) (Fig. 4c) or Eqs. (24) and (25) (Fig. 4d). If the A_z' term in y of Eq. (22) is considered (Fig. 4c), the differences between the pseudo-3D and true-3D models persist from the anticlinal hinge to the footwall area. In the footwall area, the beds of the true-3D model are displaced upwards relative to the beds of the pseudo-3D model, and this upward displacement increases away from the fault (Fig. 4c). Footwall regions away from the fault that at some point in the deformation were inside the triangular zone of shear and had high x values, experienced high velocity in the **y** direction (Eqs. (22) and (23)). If the A_z' term in y of Eq. (22) is not considered (Eqs. (24) and (25), Fig. 4d), the differences between the pseudo-3D and true-3D models are concentrated in the anticlinal hinge area and, contrary to the model of Fig. 4c, decrease away from the fault. Notice also that in the true-3D models, the backlimb of the anticline dips gently away from the anticlinal hinge area, as opposed to the backlimb of the pseudo-3D model which is flat (Fig. 4c, d).

Analogous simulations to those of Fig. 4, for a 60° dipping normal fault show similar differences between the pseudo-3D (black lines) and true-3D (gray lines) models (Fig. 5). The differences are mainly due to the different orientation of the **xyz** coordinate system of the pseudo-3D and true-3D models (Fig. 5a, c, and d). However, compared to the reverse fault simulations (Fig. 4), the differences between the pseudo-3D and true-3D models in the folded area of the normal fault simulations (Fig. 5) are almost insignificant. This is because in the normal fault simulations the trishear zone is at higher angle to bedding and therefore moves faster through the beds (i.e. bed particles spend less time inside the trishear zone). Also, if at any stage of the deformation bed particles are inside the triangular zone, they are close to the tip line (low x values), which is the area in which the pseudo-3D and true-3D models differ less (Fig. 2).

4.2. Lateral fault propagation

Lateral fault propagation with $(P/S)_l$ greater than P/S is a special case in which the slip gradient along the fault (A_v) and the obliquity of the tip line with respect to strike (α) decrease with deformation. At the beginning of the deformation the length of the tip line is short, the slip at one tip is non-zero and at the opposite tip is zero. A_v and the incremental change of α are high. As slip accumulates and the fault grows in length along strike faster than it propagates across strike, A_v and α decrease. In terms of a comparison between pseudo-3D and true-3D models, maximum differences between the models exist at the beginning of the deformation and the differences decrease as deformation proceeds.

Fig. 6 shows lateral fault propagation models of 30° dipping reverse (left side) and 60° dipping normal (right side) faults. In both, the reverse and normal fault simulations, the trishear angle is 60°, the magnitude of cumulative slip varies from 250 units at T_s to 0 at T_n, the slip is accumulated over 125 slip increments (magnitude of slip = 2 units at T_s and 0 at T_n), the P/S is 1.5, the $(P/S)_l$ is 3.0, and the initial fault length along strike is 50 units. The fault propagates twice as fast in the strike direction as in the up-dip direction.

Topographic contours on the deformed bed of the pseudo-3D (Fig. 6a), true-3D using Eqs. (22) and (23) (Fig. 6b), and true-3D using Eqs. (24) and (25) (Fig. 6c) models, illustrate a complex displacement field, with maximum relief and maximum dip of the forelimb at T_s and decreasing towards T_n. There are differences between the pseudo-3D and the true-3D simulations in the hanging wall, forelimb, and footwall areas. In the hanging wall, the elevation contours of the pseudo-3D model are parallel to the slip vector (i.e. perpendicular to fault strike, Fig. 6a), while those of the true-3D models are oblique to the slip vector (Fig. 6b, c). In cross sections perpendicular to strike, the hanging wall area is flat in the pseudo-3D model (Fig. 6a), but dips towards the hanging wall in the true-3D models (Fig. 6b, c). This is because in the true-3D models the orientation of the **xyz** coordinate system changes progressively with deformation, resulting in a richer kinematics in the hanging wall. In the forelimb area the bed is steepest in the pseudo-3D model (Fig. 6a), and least steep in the true-3D simulation using Eqs. (22) and (23) (Fig. 6b). In the footwall, the elevation contours of the pseudo-3D model return in a relatively short distance to the regional elevation of the bed (Fig. 6a), while in the
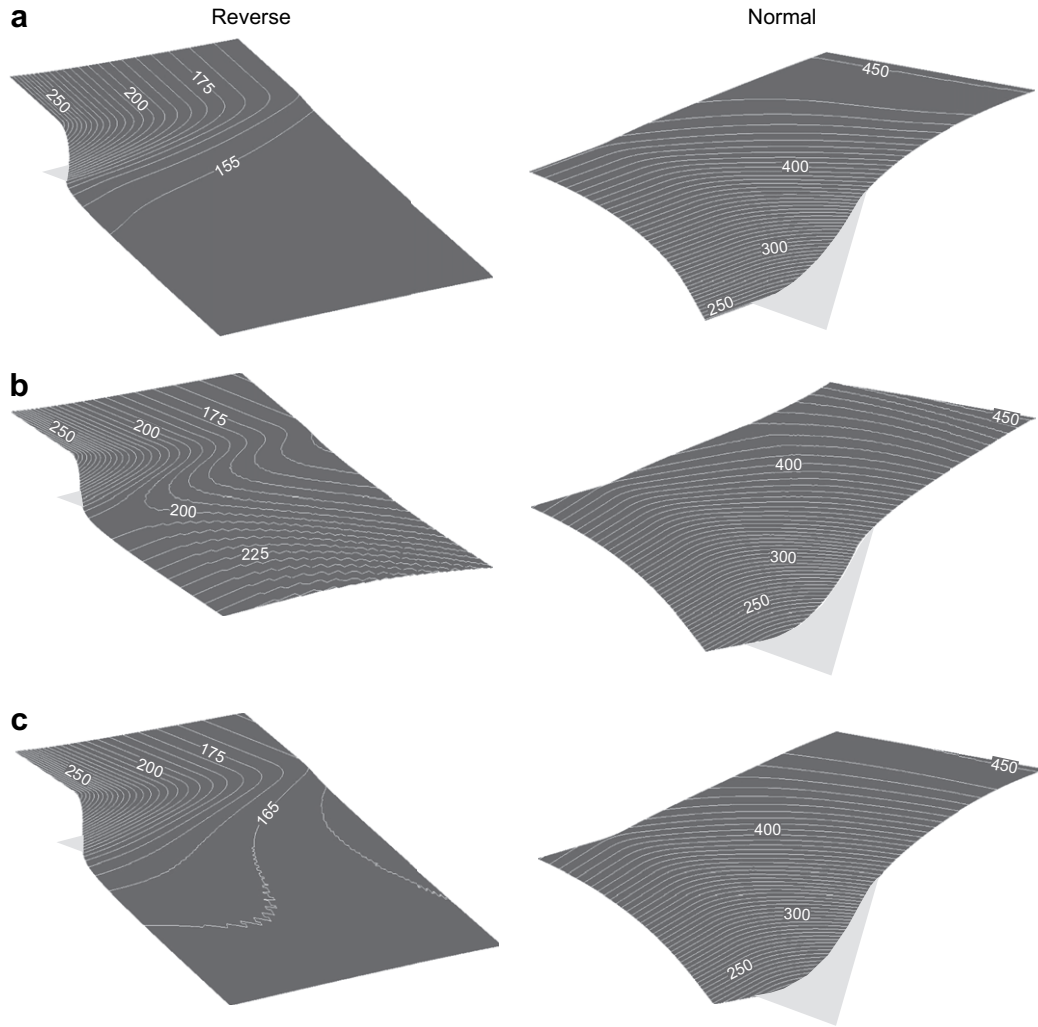
Fig. 6. 3D trishear models of laterally propagating, reverse (left side) and normal (right side) faults for (a) pseudo-3D, (b) true-3D using Eqs. (22) and (23), and (c) true-3D using Eqs. (24) and (25) models. White contours on the deformed bed are elevation.

true-3D models the footwall experiences upward displacement (Fig. 6b, c). This upward displacement is significant in the model in which the A_z' term in y of Eq. (22) is considered (Fig. 6b). In this case footwall areas away from the fault that at some point in the deformation were inside the triangular zone and had high x values, experienced high velocity in the **y** direction (Eqs. (22) and (23)). In the model in which the A_z' term in y of Eq. (22) is not considered (Fig. 6c), the upward displacement of the footwall is less significant and the footwall topography is closer to that of the pseudo-3D model (Fig. 6a).

4.3. Volume conservation

In this section, I check the correctness of the pseudo-3D and true-3D models by computing the change of volume of a representative group of 3D simulations, including those of Figs. 4–6. If a pseudo-3D or true-3D model is correct, it should preserve volume. The change of volume was computed by measuring the initial and final volume between two beds that are not cut by the fault and that initially were flat and vertically separated by a distance of 25 units. The volume between the beds was estimated by subtracting the volumes of the upper and lower beds to a datum. The volume from a bed to the datum was computed by summing up the volume contribution of each of the quadrilateral cells that make the bed, mainly the average area of the quadrilateral times the average height of the quadrilateral to the datum. Clearly, there are errors in the computation. These errors increase with the tightness of the fold and the magnitude and relative variation of dip of its forelimb.

Fig. 7 shows the percent, relative volume change (difference of final and initial volume divided by initial volume), of pseudo-3D and true-3D simulations of 30° reverse (white area) and 60° normal (gray area) faults. All models have slip perpendicular to fault strike (R is 90°). This facilitates the computation of volume change. Models NV (no variation of trishear parameters along strike), TAV (variation of trishear angle along strike, Figs. 4b and 5b), NP (no fault propagation but variation of slip along strike), and VPS (variation of P/S along strike, Figs. 4a and 5a), are all cases in which the
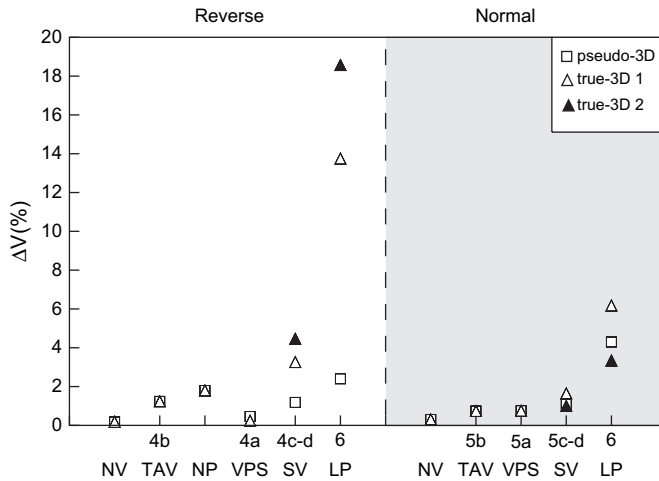
Fig. 7. Percent volume change of different pseudo-3D (squares) and true-3D (triangles) trishear models of reverse (white area) and normal (gray area) faults. First row of labels of the horizontal axis indicate the corresponding model's figure in the paper. Initials in the second row of labels of the horizontal axis correspond to: NV, no variation of trishear parameters along strike; TAV, variation of trishear angle along strike; NP, zero propagation and variation of slip along strike; VPS, variation of P/S along strike; SV, variation of slip along strike; and LP, lateral fault propagation. In models SV and LP, non-filled triangles correspond to true-3D models computed using Eqs. (22) and (23), and filled triangles to true-3D models computed using Eqs. (24) and (25).

true-3D implementation contains no inconsistencies (A_z' is zero, Section 2). These true-3D trishear models (triangles in Fig. 7) should yield no volume change. This is not exactly the case in Fig. 7 because of errors in the volume change computation which can be up to 2% (model NP). Notice that in the NV to VPS simulations the volume change of pseudo-3D models (squares in Fig. 7) and true-3D models (triangles in Fig. 7) is practically the same, even in the VPS simulation (Figs. 4a and 5a) where the pseudo-3D and true-3D models have different solution **xyz** coordinate systems (Section 3). True-3D and pseudo-3D models preserve volume in the NV to VPS simulations.

In simulations with variable slip along strike, SV (variation of slip along strike, Figs. 4c, d and 5c, d) and LP (lateral fault propagation, Fig. 6), the volume change of true-3D models can be considerable, particularly in reverse faults (Fig. 7). This is because in the SV and LP simulations, A_z' is not zero (Section 2). In the reverse fault, SV simulation, for an along-strike slip gradient (A_v) of 0.002, the volume change of pseudo-3D (squares in Fig. 7), true-3D using Eqs. (22) and (23) (non-filled triangles in Fig. 7), and true-3D using Eqs. (24) and (25) (filled triangles in Fig. 7) models, is 1.2, 3.3, and 4.5%, respectively. The volume change becomes more significant for higher A_v values. For example, for A_v of 0.003, the volume change is 1.7, 6.3, and 8.7%, respectively. Notice that in both cases, the volume change of the pseudo-3D implementation is below the 2% resolution limit of the computation. The pseudo-3D formulation preserves volume in the SV simulation, but the true-3D formulation does not. Volume changes of the true-3D formulation are to a certain degree acceptable in normal fault simulations and in reverse fault simulations with low slip

gradients ($A_v < 0.002$, Fig. 4c, d). True-3D models with higher slip gradients have significant volume changes and are questionable.

The LP (lateral fault propagation, Fig. 6) simulation is the most challenging and where volume changes are more evident (Fig. 7). Volume change in the LP reverse fault simulation for the pseudo-3D, true-3D using Eqs. (22) and (23), and true-3D using Eqs. (24) and (25) models, is 2.4, 13.7, and 18.6%, respectively. In the LP normal fault simulation, the volume change is 4.3, 6.2, and 3.3%, respectively. Volume changes of the pseudo-3D formulation are to some extent acceptable, specially if one considers that errors in the volume change computation can be significant. Volume changes of the true-3D formulation are acceptable in the LP normal fault simulation (the true-3D model using Eqs. (24) and (25) yields in fact lower volume changes than the pseudo-3D model, Fig. 7), but definitely not acceptable in the LP reverse fault simulation. In this case, the true-3D formulation is questionable.

5. Discussion

The algorithms and implementation strategies presented in this note provide a versatile kinematic framework to model the 3D geometry and finite strain of reverse and extensional fault propagation folds. Along strike changes of fault parameters, oblique slip, up-dip and/or along strike fault propagation, produce complex pre-growth and growth bed geometries, and complex finite strain fields. There is, however, one limitation. The pseudo-3D and true-3D algorithms can only model fault propagation folding ahead of planar, constant dip faults. Folding in front of faults that change in dip along strike cannot be modeled. Backlimb folding due to non-planar, multi-bend faults can be modeled using simple kinematic models such as layer parallel slip or inclined shear. This option is implemented in my Trishear3D program.

Of the two existent algorithms to model trishear in three-dimensions, the pseudo-3D algorithm is the most efficient and most versatile. The fact that the solution coordinate system of the pseudo-3D algorithm is independent of the current orientation of the tip line, makes the computation faster and allows the introduction of more complex variations of trishear parameters than the standard linear variation between the fault tips. Although an ad-hoc implementation, the pseudo-3D algorithm preserves volume within acceptable limits in all situations, even in the most exigent simulation such as lateral fault propagation (Fig. 7). This conclusion is equally valid for faults with slip perpendicular (this note), or oblique to strike. The pseudo-3D algorithm is a fast and correct method to model trishear in three-dimensions, and should be considered as a first option when dealing with inversion problems (i.e. finding the trishear parameters that best fit a real structure), which require the testing of thousands of trishear simulations.

A solution coordinate system that does not change in orientation with deformation, such as in the pseudo-3D model, produces a very simple hanging wall geometry. Even in cases in which the fault slip varies along strike, the elevation contours of the hanging wall of a pseudo-3D model are parallel to the

slip vector (the hanging wall is flat in cross sections parallel to the slip vector, Figs. 4c, d and 6a). This may be an oversimplification. Analogue models of laterally propagating reverse faults, show that the elevation contours of the hanging wall are oblique to the slip vector (Fischer and Keating, 2005, their Fig. 10). Outcrop observations of The Rip Van Winkle anticline in New York (USA), a reverse fault propagation fold produced by a fault with suspected variation of slip along strike, show a backlimb that dips away from the anticlinal hinge area in sections parallel to the slip vector (Cardozo et al., 2005). These observations are better reproduced by the true-3D formulation. In this formulation, the solution coordinate system progressively rotates and follows the orientation of the tip line, resulting in a more complex hanging wall geometry and, in the case of variable slip models, a fold backlimb that dips away from the anticlinal hinge area (Figs. 4c, d and 6b, c).

The true-3D algorithm, however, produces volume changes in simulations with variable slip along strike. These volume changes are significant in reverse fault simulations with high slip gradient along strike and high obliquity of the tip line with respect to the slip vector and/or the fault strike, such as lateral fault propagation (Fig. 7). Volume changes in the true-3D algorithm are explained by mathematical inconsistencies in both the triangular zone of shear and the hanging wall area above it. These inconsistencies become evident when A_z' (Eq. (17)) is not zero (Section 2). Volume changes due to inconsistencies inside the triangular zone, can be assessed by comparing true-3D models in which the A_z' term in y of Eq. (22) is considered (at least partially correct in the hanging wall area of the triangular zone), or not. True-3D, reverse fault, variable slip models that consider the A_z' term in y (Figs. 4c and 6b) have about 30% less volumetric change than corresponding true-3D models that do not consider the A_z' term in y (Figs. 4d and 6c, Fig. 7). This suggests that the mathematical inconsistencies inside the triangular zone account for about 30% of the total volume change. It also suggests that, in terms of volume conservation, it is better to consider the A_z' term in y (Eqs. (22) and (23), Cristallini et al., 2004). Nonetheless, true-3D models that consider the A_z' term in y are incompatible at the lower boundary of the triangular zone (Section 2), and produce extreme upward deformation in the footwall area away from the fold (Fig. 6b). In my opinion, not considering the A_z' term in y (Eqs. (24) and (25)) is the best way to deal with the inconsistencies of the true-3D model inside the triangular zone of shear.

That volume changes in the hanging wall area above the triangular zone account for a considerable percent (about 70%) of the total volume change in variable slip, true-3D models, can be seen in Fig. 8. This figure shows the dilation of the reverse, lateral fault propagation model of Fig. 6 for the pseudo-3D (Fig. 8a), true-3D using Eqs. (22) and (23) (Fig. 8b), and true-3D using Eqs. (24) and (25) (Fig. 8c) simulations. The dilation (i.e. finite strain) was computed using the initial and final geometry of tetrahedrons embedded in the layer. The computation is described in detail by Williams and Kane (1999). In the pseudo-3D model, negative dilation is confined to a small area in the forelimb, while in the rest of the structure there is no dilation (Fig. 8a). To the contrary, in the true-3D models the dilation
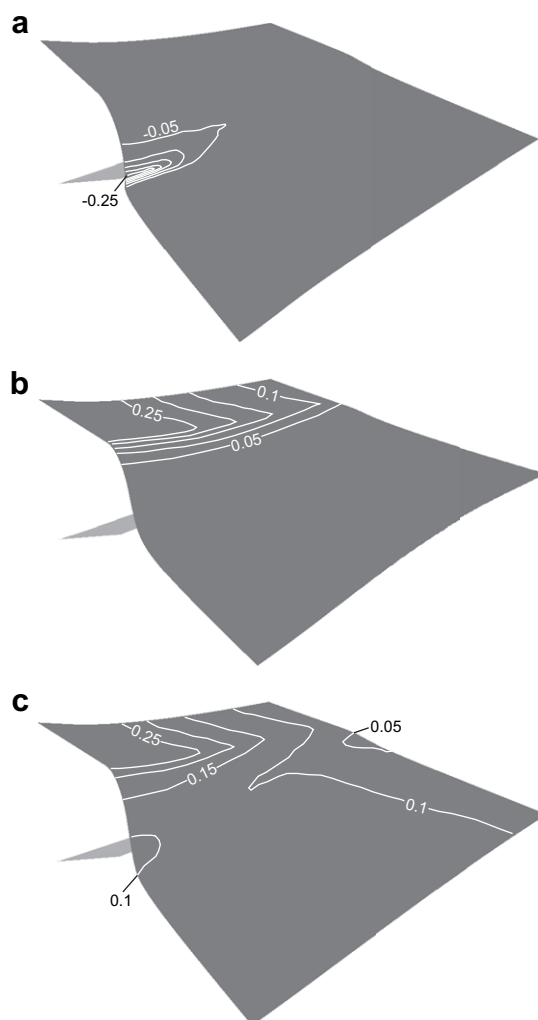
Fig. 8. Dilation contours for the reverse fault, lateral propagation simulations of Fig. 6. (a) Pseudo-3D, (b) true-3D using Eqs. (22) and (23), and (c) true-3D using Eqs. (24) and (25) simulations.

in the hanging wall is considerable. It is positive and larger than the dilation in the forelimb and footwall areas (Fig. 8b, c). Volume changes in the hanging wall of the true-3D models are larger than those of the forelimb and footwall areas. In these areas, the dilation is higher in the true-3D model using Eqs. (24) and (25) (Fig. 8c), than in the true-3D model using Eqs. (22) and (23) where the dilation approaches zero (Fig. 8b). This explains why variable slip, true-3D models using Eqs. (22) and (23) yield less volume change than corresponding true-3D models using Eqs. (24) and (25).

Volume changes such as those predicted by the true-3D models of Fig. 8b, c may occur in nature under high slip obliquity and slip gradients, for example during strike slip faulting. In nature, these volume changes are resolved by subordinate folding and faulting, differential compaction, and dissolution; processes that are not included in the pseudo-3D or true-3D formulations.

This note examines the implementation and mathematical consistency of the existent trishear 3D formulations. A more fundamental question is how these formulations compare to reality. Implementing efficient inverse 3D trishear modeling strategies to fit real structures, and comparing the predicted

geometries and strain fields of 3D trishear models with the geometries, distribution of mesostructures (i.e. fractures), and petrophysical properties of faulted and folded reservoirs, are important topics for future research.

Acknowledgments

References

Allmendinger, R.W., 1998. Inverse and forward numerical modeling of trishear fault-propagation folds. Tectonics 17, 640–656.

Allmendinger, R.W., Zapata, T.R., Manceda, R., Dzelalija, F., 2004. Trishear kinematic modeling of structures, with examples from the Neuquén Basin, Argentina. In: McClay, K. (Ed.), Thrust Tectonics and Hydrocarbon Systems. Memoir, vol. 82. American Association of Petroleum Geologists, pp. 356–371.

Cardozo, N., Allmendinger, R.W., Morgan, J.K., 2005. Influence of mechanical stratigraphy and initial stress state on the formation of two fault propagation folds. Journal of Structural Geology 27, 1954–1972.

Cristallini, E.O., Allmendinger, R.W., 2001. Pseudo-3D modeling of trishear fault-propagation folding. Journal of Structural Geology 23, 1883–1899.

Cristallini, E.O., Giambiagi, L., Allmendinger, R.W., 2004. True three-dimensional trishear: a kinematic model for strike-slip and oblique-slip deformation. Geological Society of America Bulletin 116, 938–952.

Erslev, E.A., 1991. Trishear fault-propagation folding. Geology 19, 617–620.

Fischer, M.P., Keating, D.P., 2005. Photogrammetric techniques for analyzing displacement, strain, and structural geometry in physical models: application to the growth of monoclinal basement uplifts. Geological Society of America Bulletin 117, 369–382.

Hardy, S., Allmendinger, R.W. Trishear: a review of kinematics, mechanics and applications. In: McClay, K., Shaw, J.H., Suppe, J. (Eds.), Thrust Fault Related Folding, American Association of Petroleum Geologists, Memoir, submitted for publication.

Williams, G.D., Kane, S.J., 1999. Three-dimensional restoration algorithm and finite strain in thrust systems. In: Thrust Tectonics 99, Conference Programme. University of London, London, UK, pp. 32–34.

Zehnder, A.T., Allmendinger, R.W., 2000. Velocity field for the trishear model. Journal of Structural Geology 22, 1009–1014.